eprints@whiterose.ac.uk
https://eprints.whiterose.ac.uk/

UV Photodissociation Dynamics of CHI$_2$Cl and its Role as a Photolytic Precursor for a Chlorinated Criegee Intermediate

Kara M. Kapnas, Benjamin W. Toulson,[1] Elizabeth S. Foreman,[2] Sarah A. Block, and Craig Murray[3]

Department of Chemistry, University of California, Irvine, Irvine CA 92697, USA

J. Grant Hill[4]

Department of Chemistry, University of Sheffield, Sheffield S3 7HF, UK

[1] Current address: Chemical Sciences Division, Lawrence Berkeley National Laboratory, Berkeley, California 94720, USA.
[2] Current address: Department of Chemistry, Massachusetts Institute of Technology, Cambridge, MA 02139, USA
[3] Email: craig.murray@uci.edu; Telephone: +1-949-824-4218
[4] Email: grant.hill@sheffield.ac.uk; Telephone: +44-(0)114-222-9392

1

Abstract

Photolysis of geminal diiodoalkanes in the presence of molecular oxygen has become an established route to the laboratory production of several Criegee intermediates, and such compounds also have marine sources. Here, we explore the role that the trihaloalkane, chlorodiiodomethane (CHI_2Cl), may play as a photolytic precursor for the chlorinated Criegee intermediate ClCHOO. CHI_2Cl has been synthesized and its UV absorption spectrum measured; relative to that of CH_2I_2 the spectrum is shifted to longer wavelength and the photolysis lifetime is calculated to be less than two minutes. The photodissociation dynamics have been investigated using DC slice imaging, probing ground state I and spin-orbit excited I* atoms with 2+1 REMPI and single-photon VUV ionization. Total translational energy distributions are bimodal for I atoms and unimodal for I*, with around 72% of the available energy partitioned in to the internal degrees of freedom of the CHICl radical product, independent of photolysis wavelength. A bond dissociation energy of $D_0 = 1.73 \pm 0.11$ eV is inferred from the wavelength dependence of the translational energy release, which is slightly weaker than typical C–I bonds. Analysis of the photofragment angular distributions indicate dissociation is prompt and occurs primarily via transitions to states of A'' symmetry. Complementary high-level MRCI calculations, including spin-orbit coupling, have been performed to characterize the excited states and confirm that states of A'' symmetry with highly mixed singlet and triplet character are predominantly responsible for the absorption spectrum. Transient absorption spectroscopy has been used to measure the absorption spectrum of ClCHOO produced from the reaction of CHICl with O_2 over the range 345–440 nm. The absorption spectrum, tentatively assigned to the *syn* conformer, is at shorter wavelengths relative to that of CH_2OO and shows far weaker vibrational structure.

Introduction

Organoiodine compounds are photochemical precursors for iodine atoms in the atmosphere and oxides of iodine play an important role in catalytic depletion of tropospheric ozone and new particle formation.[1,2] Oceans are the major source of organoiodine compounds, which are particularly important species in the marine boundary layer (MBL)[3,4]. Methyl iodide (CH_3I) is the most prevalent organoiodine compound in the MBL, although some dihalomethanes such as diiodomethane (CH_2I_2), which have absorption spectra that extend to longer wavelengths and shorter photolysis lifetimes, are larger contributors to the marine I atom flux.[5] Recent work has suggested that trihalomethanes could also be I atom precursors in the marine atmosphere. Liss and coworkers found chlorodiiodomethane (CHI_2Cl) and dibromoiodomethane ($CHIBr_2$) were present after several species of macroalgae in coastal seawater obtained around Mace Head, Ireland were incubated for several hours.[4] More recently, reactions of dissolved organic matter with HOI and/or I_2, generated at the ocean surface through the oxidation of iodide by ozone, has been suggested as a ubiquitous sea-surface source of the trihalomethanes chlorodiiodomethane and iodoform (CHI_3).[6]

The gas-phase photodissociation dynamics of organoiodine compounds has a long history. CH_3I in particular is well studied, and a good summary can be found in a recent article by Gardiner et al.[7] The A band of CH_3I peaks near 257 nm and results from $\sigma^* \leftarrow n$ excitation. Absorption at wavelengths near the band maximum occurs primarily via a parallel transition to the repulsive $^3Q_1$ state which correlates with spin-orbit excited $I^*(^2P_{1/2})$ atoms. The small fraction of ground state $I(^2P_{3/2})$ atoms result from surface-hopping via an exit channel conical intersection. The fraction of the available energy partitioned into relative translation, f_T, of the CH_3 and I products is around 0.7–0.8. The subset of iodine-containing dihalomethanes CH_2XY (X = I, Y = Cl, Br, I) present different photochemistry, although the long-wavelength absorption bands still arise from $\sigma^* \leftarrow n$ excitations localized on the C–I chromophore and lead predominantly to cleavage of the C–I bond.[8]

$$CH_2IY + h\nu \rightarrow CH_2Y + I(^2P_{3/2}) \tag{R1a}$$

$$\rightarrow CH_2Y + I^*(^2P_{1/2}) \tag{R1b}$$

For the mixed dihalomethanes, CH_2ICl and CH_2IBr, the long wavelength absorption spectra are like that of CH_3I but the absorption maxima at ~270 nm lies to longer wavelength. Excitation in the A bands is due to transitions that are localized on the C–I bond and lead predominantly to formation of I atoms. For CH_2ICl the transitions localized on the C–Cl chromophore that lead to C-Cl bond cleavage lie significantly higher in energy and dissociation proceeds exclusively by C–I bond cleavage.[9–13] In contrast, Br atoms are also formed as a minor channel following photolysis of CH_2IBr in the A band, an observation primarily attributed to simultaneous weak excitation of the partially overlapped higher lying transition that is localized on the C–Br bond.[14,15] In both CH_2ICl and CH_2IBr, dissociation occurs via strongly parallel transitions, with a reduced propensity for I* and a smaller fraction of the available energy partitioned into translation (f_T ~0.4) than for CH_3I. The addition of a second C–I chromophore and reduction in symmetry leads to the appearance of additional bands in the near-UV absorption spectrum of CH_2I_2, which extends to longer wavelengths.[16,17] The electronic structure of CH_2I_2 has been described qualitatively using an exciton model[8] as well as theoretically using *ab initio* calculations that include effects of spin-orbit coupling and show that excited states with heavily mixed singlet and triplet character are responsible for the absorption spectrum.[18,19] Photolysis of gas phase CH_2I_2 in the near-UV leads to energy being partitioned predominantly into internal excitation of the iodomethyl (CH_2I) radical rather than translation, with f_T reduced to ~0.2.[8,18,20–25] The I* yield is effectively zero following excitation at longer wavelengths, but steadily increases to almost 0.5 at 248 nm.[21,22] The photochemistry of dihalomethanes has also been studied in condensed phases using ultrashort laser pulses, with transient absorption measurements leading to the suggestion that the $CH_2I–Y$ isomer is formed on short timescales.[26–30] In contrast to the dihalomethanes, little work has been done on trihalomethanes.

Interest in the photochemistry of CH_2I_2 has been re-invigorated recently by its use as a precursor for the laboratory synthesis of the Criegee intermediate formaldehyde oxide, CH_2OO. Criegee intermediates, R_1R_2COO, are important reactive species in the troposphere formed by alkene ozonolysis; the energized intermediates can decompose to form hydroxyl radicals, while those that are stabilized by collisions react with trace species, in some cases leading to particle formation.[31–35] Photolysis of CH_2I_2 in the presence of O_2 was first demonstrated by Welz et al.[36] to be an efficient route to generate CH_2OO in sufficient concentration for kinetics studies at low pressure, following initial work by Eskola et al. who had identified I atom formation in the $CH_2I + O_2$ reaction.[37] The CH_2OO yield in the $CH_2I + O_2$ reaction approaches unity at low pressure, decreasing to ~30% at atmospheric pressure.[38–40] The UV absorption spectrum of CH_2OO has been measured using several spectroscopic techniques.[41–44] Photolysis of larger geminal diiodoalkanes to produce iodoalkyl radicals which can subsequently react with O_2 has been used successfully to produce larger Criegee intermediates.[45,46] While the major source of most Criegee intermediates in the atmosphere is alkene ozonolysis, the photolytic production of iodoalkyl radicals could also contribute in regions such as the MBL where precursor concentrations are elevated. Halogen-substituted alkenes react extremely slowly with ozone, with rate constants typically $<10^{-19}$ cm^3 molecules^{-1}.[47,48] Iodoalkyl radicals with additional halogen substituents may be an alternative source of halogenated Criegee intermediates.

In this paper, we report the UV absorption spectrum and near-UV photochemistry of the trihalomethane CHI_2Cl, which we hypothesize could act as a photolytic precursor for the chlorinated Criegee intermediate ClCHOO by way of chemistry analogous to that of CH_2I:

$$CHICl + O_2 \rightarrow ClCHOO + I \tag{R2}$$

Recently, Cabezas et al. have produced ClCHOO in a pulsed electrical discharge and measured the rotational spectra of both anti and syn conformers using Fourier-transform microwave spectroscopy.[49] Calculations suggest that syn-ClCHOO is more stable by 1088 cm^{-1} (0.1349 eV)

without zero-point corrections. The photodissociation dynamics of CHI_2Cl in the wavelength range 355–266 nm has been studied using DC slice velocity-map ion imaging, probing I and I* atoms using 2+1 resonance-enhanced multiphoton ionization and single-photon vacuum ultraviolet (VUV) ionization. The experimental measurements are complemented by high-level multi-reference electronic structure calculations, including effects of spin-orbit coupling, that characterize the excited electronic states of CHI_2Cl responsible for the absorption spectrum and the dissociation dynamics. Broadband transient absorption spectroscopy experiments demonstrate that the reaction of the CHICl radical photoproduct with molecular oxygen leads to formation of the ClCHOO Criegee intermediate. The absorption spectrum of ClCHOO in the wavelength range 345–440 nm is also reported and tentatively assigned as being predominantly due to the *syn* conformer.

Experimental and theoretical methods

1. CHI_2Cl synthesis and characterization

CHI_2Cl, commonly used as a precursor for forming halogenated cyclo-propanes,[50,51] is not commercially available and was therefore synthesized using the procedure described by Li *et al.*[52] Chloroform (223 mL, 1.25 mol), triethylbenzylammonium chloride (TEBA) (5.0 g, 21.9 mol), a 50% NaOH solution (110 g, 2.75 mol) in water (220 mL), and a solution of NaI (500 g, 3.34 mol) in water (490 mL) were added to a round bottom flask. The reaction mixture was then heated to 65 °C for 24 h. After cooling, the mixture was poured into water (3 L) and extracted with CH_2Cl_2 (1 L × 4). The organic layer was washed with saturated Na_2SO_3 solution, dried over Na_2SO_4, and concentrated. The crude reaction mixture was redistilled to provide the product as a light sensitive red liquid (136.5 g, 16%). ^{1}H and ^{13}C NMR spectra were consistent with those previously reported for this compound. The vapor pressure of CHI_2Cl at 294 K was determined by connecting an airtight glass vessel containing CHI_2Cl to a static cell and monitoring the pressure increase. To obtain the gas phase absorption spectrum, a small sample of CHI_2Cl was added to a sealed quartz cuvette and allowed to

equilibrate. The UV absorption spectrum was measured from 190–400 nm at 294 K using a UV-visible spectrometer (Cary 50).

2. DC slice velocity-map slice ion imaging

Photodissociation experiments were performed in a DC slice velocity-map imaging (VMI) spectrometer. The main characteristics of the setup have been described previously.[18] A liquid sample of CHI_2Cl stored in a stainless steel bubbler was seeded in argon (approximately 1% CHI_2Cl) at 1 atm backing pressure and was supersonically expanded using a pulsed nozzle (General Valve Series 9) and skimmed (Beam Dynamics Inc.) to form a molecular beam. The molecular beam is directed along the time-of-flight axis into the ionization chamber and intersected perpendicularly by counter-propagating photolysis and probe laser beams in the center of velocity-mapping electrodes, optimized for DC slicing. A tunable mid-band optical parametric oscillator pumped by a Nd:YAG laser (Continuum Horizon II and Surelite EX) was used to generate the photolysis beam in the wavelength range 266–355 nm. The photolysis beam was focused using a fused silica lens (f = 300 mm). Nascent I and I* photofragments were probed approximately 30 ns after photolysis via single-photon VUV ionization or 2+1 REMPI using a Nd:YAG pumped frequency doubled dye laser (Lambda Physik Scanmate II and Continuum Surelite II-10). VUV radiation at 118.2 nm was generated by frequency tripling the 3rd harmonic of a Nd:YAG laser in a gas mixture of Xe and Ar. The REMPI probe beam was generated by frequency doubling the fundamental output of a Nd:YAG-pumped dye laser. To avoid non-resonant multi-photon dissociation induced by the probe laser, the pulse energy did not exceed ~0.5 mJ. The ions were accelerated towards a detector comprising microchannel plates and a phosphor screen (Photonis). A fast, high voltage pulser (Photek GM-MCP-2) allows imaging of only the narrow central slice of the ion Newton sphere. Detector phosphorescence was captured using a CCD camera (Basler a312f) interfaced to a PC running custom data acquisition software (National Instruments LabVIEW) that performs centroiding and ion-counting.

7

3. Broadband Transient Absorption Spectroscopy

Experiments were performed in a flash photolysis, single-pass transient absorption flow cell apparatus that has been described in detail previously.[44,53] A pulsed Nd:YAG laser was used to photodissociate CHI_2Cl in the presence of excess O_2 at 355 nm and 266 nm (7±1 mJ pulse^{-1}). Spectra were recorded at 15 Torr total pressure with the gas mixture comprising 0.02% CHI_2Cl, 10% O_2 and N_2 balance. All gas flows were regulated by calibrated mass flow controllers (Alicat). Absorption spectra were measured over the range of 345–440 nm using probe LEDs nominally centered at 345 nm, 365 nm and 405 nm, each spanning 20–30 nm. The LEDs were pulsed at maximum brightness for up to 6 μs using a high-current driver (LightSpeed Technologies, HPLS-36). The broadband LED output was coupled into a fiber optic and collimated using an achromatic doublet. The photolysis laser and probe LED beams were overlapped along the complete 50 cm length of the flow cell using dichroic mirrors chosen to transmit probe light to the red of the photolysis laser wavelength. The transmitted probe light was dispersed in a spectrometer operated with a resolution 2.2 nm and coupled to a low-noise, cooled CCD detector (Andor SR303i and iDus 420). Spectra were collected at a 10 Hz repetition rate with a 30 μs delay between photolysis and LED pulses.

4. *Ab initio* calculations

The geometry of CHI_2Cl was optimized for the ground electronic state using the explicitly correlated coupled cluster with single, double and perturbative triple excitations [CCSD(T)-F12b] method.[54,55] The cc-pVTZ-F12 basis set was used for hydrogen, carbon and chlorine,[56] with the cc-pVTZ-PP-F12 basis set and ECP28MDF small-core relativistic pseudopotential for iodine.[57,58] The MP2Fit and OptRI auxiliary basis sets specifically matched to these orbital basis sets were utilized in the density fitting of most of the two-electron integrals and in the resolution-of-the-identity, respectively.[57,59,60] Density fitting of the Fock and exchange matrices used the cc-pVTZ/JKFit and def2-QZVPP/JKFit auxiliary sets.[61,62] The geminal Slater exponent was set to 1.0 a_0^{-1} throughout, and the complementary

auxiliary basis set (CABS) singles correction was computed and added to the reference energy.[61,62] The absorption spectrum of CHI_2Cl and potential energy curves along the C–I bond coordinate were calculated using the explicitly correlated multi-reference configuration interaction method with the Davidson correction (MRCI-F12+Q),[63–65] along with the double-zeta variants of the orbital and auxiliary basis sets detailed above. The complete-active-space self-consistent field (CASSCF) reference for these calculations consisted of 12 electrons in 10 orbitals (6 A$'$ and 4 A$''$ in C_s symmetry), which was determined by inspecting the natural orbitals from full-valence CASSCF calculations and removing any orbitals from the active space that had occupations greater than 1.95 for both the equilibrium geometry and a geometry where the C–I distance had been elongated to 4.2 Å. The vertical excitation energies of the first 11 excited states (3 × ^{1}A$'$, 2 × ^{1}A$''$, 3 × ^{3}A$'$, and 2 × ^{3}A$''$) were calculated. Spin-orbit coupling calculations were conducted on these 11 spin-free states using two different methodologies: (i) The calculated absorption spectrum at the equilibrium geometry was produced at the spin-orbit MRCI level (MRCI-SO herein) using the CASSCF reference outlined above, with the cc-pVDZ basis set for hydrogen and carbon,[66] the cc-pV(D+d)Z basis for chlorine,[67] and the cc-pVDZ-PP basis and associated pseudopotential for iodine.[58] (ii) Potential energy curves were computed by scanning along a C–I bond distance (keeping all other internal coordinates fixed at the equilibrium geometry) with spin-orbit coupling calculated at the CASSCF level (CAS-SO) using analogous triple-zeta quality basis sets. In all spin-orbit coupling calculations the energy eigenvalues obtained in the preceding MRCI or CASSCF calculations were replaced by those precomputed at the MRCI-F12+Q/cc-pVDZ-F12 level, meaning only the spin-orbit matrix elements were calculated at the lower level of theory. The spin-orbit operator defined in the pseudopotential was used for iodine, with the Breit-Pauli operator used for lighter atoms. All calculations were carried out using the MOLPRO 2015.1 package of *ab initio* programs.[68,69]

Results and Discussion

1. CHI$_2$Cl absorption spectrum

The gas-phase UV absorption spectrum of CHI$_2$Cl from 220–400 nm at 294 K is shown in Figure 1(a). A vapor pressure of 0.58 torr at 294 K for CHI$_2$Cl was measured in a static gas cell, and used to determine the absolute absorption cross section by means of a simple Beer-Lambert analysis. Analogous measurements of the absorption spectrum of CH$_2$I$_2$ vapor resulted in cross sections that were in excellent agreement with previously reported values in this wavelength range.[16,17] The absorption spectrum comprises five Gaussian bands, with maxima at 349 nm, 302 nm, 264 nm, 220 nm, and 209 nm, subsequently labeled A–E, respectively. Band E, which is not shown in Figure 1, has a peak absorption cross section of 2×10^{-17} cm^2 and is the most strongly absorbing feature in the spectrum. The absorption spectrum of CHI$_2$Cl is similar to that of CH$_2$I$_2$, as shown in Figure 1(b) which is consistent with photoelectron spectroscopy measurements that have indicated that Cl–I interactions are relatively weak and has no effect on the bonding orbitals.[70] However, the absorption bands of CHI$_2$Cl are slightly shifted to longer wavelength. Band A, which appears as a shoulder in the CH$_2$I$_2$ spectrum, is distinct in the CHI$_2$Cl spectrum and has the largest shift of ~31 nm. In contrast, bands B–D are shifted by only ~15 nm. The same behavior is observed in the spectra of CH$_3$I, CH$_2$ICl, and CH$_2$IBr where addition of a Cl or Br atom causes a similar shift of ~13 nm, as shown in Figure 1(c). The red shift is likely due to stabilization of the σ* antibonding orbital, as noted by Lee and Bersohn.[14] Photoelectron spectroscopy measurements on various halomethanes have suggested that the interactions between Cl or Br atoms with I are relatively weak.[70,71] Excitation of transitions involving orbitals localized on the C–Cl chromophores are expected to lie at wavelengths significantly shorter than 190 nm.

2. CHI$_2$Cl photodissociation dynamics

The photodissociation dynamics of CHI$_2$Cl has been studied using DC slice imaging of ground state I

and spin-orbit excited I* atoms. I atoms were detected using single-photon VUV ionization at 118.2

nm following photolysis at 266 nm, 282 nm, 304 nm, 344 nm, and 355 nm. Ionization at 118.2 nm

provides a high degree of specificity for I atoms over I* due to a resonance with an auto-ionizing

Rydberg state, which results in a detection sensitivity that is 19.2 times greater.[72,73] I* atoms were

detected using 2+1 REMPI transitions near 282 nm, 304 nm, and 344 nm in one-color experiments

where the probe also acts as the photolysis beam. Direct integration (and appropriate Jacobian

transformation) of the sliced images repres0065nted in polar coordinates $I(r, \theta)$, yielded the

photofragment radial $I(r)$ and angular distributions $I(\theta)$. The pixel-to-speed conversion factor was

determined using S(^{1}D) calibration images obtained following photolysis of OCS at 235 nm. I (or I*)

atom speeds were subsequently converted into total translational energy E_T using

$$E_T = \frac{1}{2} m_I (1 + \frac{m_I}{m_{CHICl}}) v_I^2$$

where it is assumed that the co-fragment is CHICl. The angular distributions were fit to the usual

expression

$$I(\theta) \propto 1 + \beta P_2(\cos \theta)$$

where θ is the angle between the recoil velocity and the polarization of the photolysis laser and P_2 is

the second Legendre polynomial. The angular distribution is characterized by the speed-dependent

(or E_T-dependent) anisotropy parameter, β, which takes limiting values of +2 for a parallel

dissociation and –1 for a perpendicular dissociation. The available energy E_{AVL} is the difference

between the photon energy and the C–I bond dissociation energy, D_0, and is partitioned into internal

excitation of the CHICl radical fragment, E_{INT}, spin-orbit excitation of the iodine atom ($E_{SO} = 0$ for I

and 0.9426 eV for I*), and the translational energy associated with photofragment recoil, E_T:

11

$$E_{AVL} = h\nu - D_0 = E_{INT} + E_{SO} + E_T$$

The internal energy of the parent CHI_2Cl is assumed to be zero due to cooling in the supersonic expansion, and is omitted from the energy balance equation.

Overall, the results are remarkably similar to those obtained previously for CH_2I_2.[18] Figure 2 shows I atom images, total translational energy distributions, and E_T-dependent anisotropy parameters. The images comprise overlapping pairs of diffuse anisotropic rings, with radii that correspond to speeds of around 600–900 m s^{-1}. The maximum intensity for the fast-moving I atoms is found at the poles, parallel to the laser polarization axis, leading to near-limiting positive β parameters. An isotropic slow component grows in at the image centers at shorter wavelengths. The bimodal fast components of the $P(E_T)$ distributions in Figure 2 show a shift to greater E_T as the available energy increases. The equivalent data for I* atoms are shown in Figure 3. The images are dominated by a single diffuse anisotropic ring, corresponding to I* speeds in the range 500–700 m s^{-1}. At a given photolysis wavelength, I* speeds are less than those of I. For example, excitation in the B band at 304 nm results in a most probable speed for I* of 610 m s^{-1} while for I the most probable speeds are 690 m s^{-1} and 790 m s^{-1}. That I* atoms are formed with lower speeds is unsurprising, since spin-orbit excitation reduces the available energy by almost 1 eV. We note that the most probable I* speeds do not correspond directly to either of the two fast components identified using VUV ionization. The angular distributions are again characterized by near-limiting positive β parameters. No two-color I* signal could be reliably distinguished above the large one-color I* signal induced by the REMPI laser alone at photolysis wavelengths of 355 nm.

Both I and I* atoms are formed with speeds that are significantly slower than the maximum allowed by energy conservation. Over the photolysis wavelength ranges used and based on typical C–I bond dissociation energies of ~2.2 eV,[74] the maximum speeds for I atoms span 1100–1500 m s^{-1} while the equivalent range for I* is only 600–1000 m s^{-1}. At all photolysis wavelengths, the I and I* atom speeds

are smaller than v_{max}, and the total translational energy is substantially less than E_{AVL}. As with CH_2I_2 photolysis, internal excitation of the radical is significant. The $P(E_T)$ distributions obtained are decomposed by fitting the fast components to Gaussian functions. The translationally slow component that appears at short wavelength is fit to an exponentially-modified Gaussian; the origin of this component will be discussed later. The average total translational energy $\langle E_T \rangle$ associated with production of I atoms increases steadily with excitation energy from 0.41 eV to 0.68 eV; the separation between the two fast components remains fixed at around 0.20 eV. The unimodal distributions obtained detecting I* are in general slightly narrower than those obtained for I atoms with a FWHM of 0.16±0.3 eV rather than the values of 0.24±0.04 eV and 0.21±0.03 eV found for each component of the bimodal I atom E_T distributions. The trend in $\langle E_T \rangle$ is maintained however, increasing from 0.28–0.51 eV as the photolysis wavelength is decreased from 344 nm to 282 nm. Energy partitioning data is summarized in Table 1.

Determination of the C–I bond dissociation energy. As shown in Figure 4, $\langle E_T \rangle$ increases linearly with the photolysis photon energy. If the fraction of the available energy partitioned into translation, f_T, is assumed to be constant, consistent with impulsive dissociation, the energy balance equation can be re-cast as

$$\langle E_T \rangle = f_T(h\nu - E_{SO}) - f_T D_0$$

where the slope is f_T and the x-intercept is D_0. For the I atom data, a linear fit yields a slope of 0.23±0.01 and a bond dissociation energy of 1.73±0.11 eV, where the uncertainties are derived from the fit. I* measurements were made at fewer photolysis wavelengths, but result in a consistent value for the D_0 of 1.70±0.63 eV, although with significantly larger uncertainty. The fraction of energy partitioned into translation for I* production is slightly larger at 0.28±0.05. We adopt the more precisely determined value of 1.73±0.11 eV for D_0 in CHI_2Cl. A similar analysis of the E_T distributions resulting from photolysis of CH_2I_2 resulted in a C–I bond dissociation energy of 2.16±0.01 eV,[18] a

result that was in reasonably good agreement with earlier experimental measurements of 2.25±0.08 eV.[74] Weakening of the C–I bond is also predicted by theory. UCCSD calculations, using the cc-pVDZ-PP basis set for I atoms and cc-pVDZ for all others, predict C–I bond dissociation energies of 1.97 eV for CH_2I_2 and 1.71 eV for CHI_2Cl. The calculations neglect spin-orbit coupling and the quality of the agreement with experiment for CHI_2Cl is likely fortuitous. The observation of a weaker C–I bond upon Cl atom addition appears to be at odds with photoelectron spectroscopy measurements on dihalomethanes, from which it had been inferred that interactions between the Cl and I atoms were weak. However, a weaker C–I bond is consistent with the chlorine atom having a stabilizing effect on the σ^* antibonding orbital, which manifests in the absorption spectrum as a shift to longer wavelengths.

Using the experimental value of D_0, of 1.73 eV, the fraction of the available energy partitioned into translation $f_T = \langle E_T \rangle / E_{AVL}$ is independent of wavelength; f_T is 0.23 and 0.29 for I and I* atoms, respectively. This constancy occurs even though the excitation wavelengths span three distinct absorption bands and involve excitation to several electronic surfaces. The similarity of the total translational energy release suggests that the underlying electronic surfaces are topographically similar. The average internal energy of the CHICl radicals $\langle E_{INT} \rangle$ formed in conjunction with I* spans the range 0.64–1.23 eV following photolysis in the wavelength range 344–282 nm. $\langle E_{INT} \rangle$ for CHICl formed in conjunction with ground state I is even greater, varying from 1.35–2.25 eV as the photolysis wavelength is decreased from 355 nm to 266 nm. The formation of highly internally excited CHICl suggests a possible origin for the isotropic slow component that appears in the I atom images at shorter wavelengths. At 266 nm, where the slow component is most pronounced and accounts for around 70% of the I atoms detected, $\langle E_{INT} \rangle$ for CHICl radicals formed in conjunction with I atoms is 2.25 eV, which is close to typical values of D_0 for iodine-containing dihalomethanes, and significantly greater than that for CHI_2Cl. The typical FWHM of the Gaussian functions used to fit the E_T, or E_{INT}, distributions is ~0.2 eV. A fraction of the hot CHICl radicals will likely have sufficient energy to

14

undergo unimolecular dissociation to form CHCl + I even at longer photolysis wavelengths, consistent with the onset of the isotropic slow component. A slow component was also observed at shorter wavelengths in our earlier work on CH_2I_2 photolysis.[18] For CH_2I_2 photolysis, f_T was reported as decreasing from 0.24 to 0.15 for I atoms and from 0.23 to 0.19 for I* atoms following photolysis in the wavelength range 355 nm to 248 nm. However, these values were based upon the complete E_T distributions, which include significant slow components at shorter wavelengths that are likely due to secondary decomposition of hot CH_2I radicals. Including only the fast components of the E_T distributions eliminates the wavelength dependence and results in revised f_T values of 0.20±0.02 and 0.21±0.03 for I and I*, respectively. Among the dihaloalkanes, CH_2IX (X = Cl, Br, I), f_T is smallest for CH_2I_2; previous studies of the photolysis of CH_2IBr found f_T = 0.31,[15] while f_T values in the range 0.39–0.48 were measured for CH_2ICl.[12,13] The measured f_T for the trihaloalkane CHI_2Cl falls between those previously reported for CH_2I_2 and CH_2IBr.

The trend in f_T following C–I bond cleavage in the dihaloalkanes approximately follows the predictions of the impulsive model described by Busch and Wilson,[75] in which the CH_2X radical is treated as a pseudo-diatomic molecule, (CH_2)–X. The fractions of the available energy partitioned into translation, rotation and vibration are given by

$$f_T = \frac{\mu_a}{\mu_f}$$

$$f_R = (1 - f_T)\sin^2\theta$$

$$f_V = (1 - f_T)\cos^2\theta$$

where μ_a is reduced mass of the atoms involved in the breaking bond, μ_f is that of the fragments, and θ is the $I(CH_2)X$ angle, taken from *ab initio* optimized geometries. The model predicts f_T values of 0.36, 0.23 and 0.19 for CH_2ICl, CH_2IBr and CH_2I_2, respectively, which are in reasonably good agreement with the experimental measurements. According to the model, the remaining energy is

partitioned primarily into haloalkyl radical rotation. The results of the impulsive model calculations are summarized in Table 2.

The pseudo-diatomic approximation breaks down for CHI_2Cl and cannot be used to predict energy partitioning into rotation or vibration. The predicted value of $f_T = 0.15$ is however in reasonably good agreement with the experimental measurements. To estimate f_R and f_V, we turn to the modified impulsive model has been developed by Butler and co-workers. which uses the measured recoil speeds to predict the rotational energy partitioning.[76,77] Recoil is assumed to be along the direction of the breaking bond, generating orbital angular momentum, $\boldsymbol{L}$

$$\boldsymbol{L} = \boldsymbol{r} \times \mu \boldsymbol{v}_{\text{recoil}}$$

where $\boldsymbol{r}$ is the vector between the centers of mass of the photofragments, and μ is the reduced mass. Angular momentum conservation requires that the angular momentum of the radical fragment is $\boldsymbol{J} = -\boldsymbol{L}$, if the initial angular momentum of the parent molecule is zero. Treating the radical rotation classically leads to

$$f_R = \frac{\mu b^2}{I} f_T$$

where b is the impact parameter and I is the scalar moment of inertia. Values of $\mu b^2 / I$ are also collected in Table 2. For the dihalolkanes, where the heavy atoms lie in a plane, the implicit assumption that rotation is about one of the radical principal axes is holds true and I_B can be used. This model leads to f_R values that are slightly smaller than those predicted by the soft impulsive model for the dihaloalkanes when using f_T, as shown in Table 2. However, using experimental $f_{T,\text{exp}}$ values for the dihaloalkanes results in unphysical results with $f_{T,\text{exp}} + f_R > 1$. For CHI_2Cl, the decrease in the impact parameter and increase in the radical moment of inertia dramatically reduces $\mu b^2 / I$, leading to a small value of f_R and consequently, preferential partitioning into radical vibration (see

16

Table 2). We note that the impulse is not perpendicular to one of the radical principal axes for CHI_2Cl and the classical rotational energy must instead be calculated using

$$E_R = \frac{1}{2}\boldsymbol{J}^T\mathbf{I}^{-1}\boldsymbol{J}$$

where $\boldsymbol{J}$ is the rotational angular momentum vector and $\mathbf{I}^{-1}$ is the inverse of the inertia tensor for the CHICl radical, evaluated at the geometry of the parent molecule, and is not diagonal. In practice, we use the PMIFST program[78] to rotate the CHICl radical into its principal axis system and use the rotation matrix to apply the same transformation to the $\boldsymbol{r}$ and $\boldsymbol{v}_{\text{recoil}}$ vectors. Using average recoil speeds measured experimentally, E_R is calculated to range from 0.56–0.93 eV for I atoms and 0.39–0.70 eV for I* atoms, with larger values corresponding to photolysis at shorter wavelengths. On average, f_R is found to be 0.32 (0.40) and f_V is 0.45 (0.31) for I (I*) atoms.

Spin-orbit branching. Additional I atom images were acquired in one-color measurements using a 2+1 REMPI transition at 304.67 nm, near the 304.02 nm transition used to probe I*. These wavelengths correspond to excitation near the absorption maximum of the B band, as shown in Figure 1. The $P(E_T)$ distribution obtained probing I atoms state-selectively using REMPI is subtly different from that measured using single-photon VUV ionization following photolysis at 304.3 nm. The normalized $P(E_T)$ distributions obtained using REMPI detection of I and I* were used as basis functions to fit the VUV data.

$$P\big(E_{T,\text{VUV}}\big) = c_1 P\big(E_{T,I}\big) + c_2 P\big(E_{T,I^*}\big)$$

The photolysis wavelengths in the one-color measurements are constrained by the two-photon atomic resonances and differ in energy by only 9 meV. Figure 5 shows the results of the fit, which allows the coefficients c_1 and c_2 to vary, subject to the constraints that they are positive and sum to unity. The best fit of the total translational energy distribution at 304 nm obtained using VUV ionization returns $c_1 = 0.91$ and $c_2 = 0.09$. After accounting for the relative photoionization cross

17

sections, which strongly favor detection of I atoms, the yield of spin-orbit excited I* atoms is 0.65. The yield of spin-orbit excited iodine appears to be significantly larger than in the dissociation of CH_2I_2, where yields of 0.26–0.35 have been reported following excitation to the B band maximum at 290 nm.[21,22]

Angular distributions. E_T-dependent anisotropy parameters derived from fitting the I and I* angular distributions are shown in Figure 2 and Figure 3, respectively. The fast components are characterized by positive β at all photolysis wavelengths for both I and I*, confirming prompt dissociation and photofragment velocities that are preferentially parallel to the photolysis laser polarization. The component peaking near zero translational energy evident in the I atom data at shorter photolysis wavelengths, earlier attributed to secondary dissociation of CHICl radicals, has $\beta \approx 0$. The anisotropy parameters for the fast components of the E_T distributions are summarized in Table 1. For ground state I atoms, the E_T distributions are bimodal; the faster of the two components has a larger value of β, which also generally increases as the photolysis wavelength is decreased. The apparent turnover at 266 nm is likely due to contributions from the underlying anisotropic component of the speed distribution. The MPI measurement at 304 nm gives results that agree with the VUV measurement for ground state I atoms. The anisotropy parameters for I* atoms fall between the values for I atoms at 304 nm and 282 nm (and agree with the average), but the value is significantly larger at 344 nm.

The β parameter can give insight into the symmetry of the electronically excited states involved in the dissociation. In the axial recoil approximation, the β parameter for a prompt dissociation is given by

$$\beta = 2P_2(\cos \chi)$$

where χ is defined as the angle between the transition dipole moment, $\hat{\mu}$, and the Jacobi vector between the departing I atom and the center of mass of the CHICl radical, $\hat{R}$.[79] CHI_2Cl belongs to the

18

C_s point group; the plane of symmetry is defined as the x–y plane, as depicted in Figure 6. The transition dipole moments lie within the x–y plane for excitation to A′ states and along the z-axis for excitation to A″ states. Using the geometry for X̃¹′ CHI₂Cl obtained from the *ab initio* calculations, excitation to A″ states is predicted to lead to fragments with a limiting value for β of +1.87, while excitation to A′ states will result in anisotropy parameters in the range –0.99 to –0.87, for transition dipole moments aligned along the x or y axes. Positive values of β are observed at all photolysis wavelengths for both I and I* atoms, indicating that the photochemistry is dominated by excitation to repulsive states of A″ symmetry. The *ab initio* absorption spectrum calculated at the MRCI-SO level and shown in Figure 7 supports the experimental inference, showing the long wavelength absorption to be dominated by absorption to the 2A″, 3A″ and 4A″ states (see also Table 3).

Potential energy curves. Extension of a C–I bond reduces the point group symmetry to C_1, allowing all states to mix and making MRCI calculations including spin-orbit coupling (MRCI-SO) unaffordable for calculating the potential energy curves along the dissociation coordinate. Figure 8 shows potential energy curves calculated spin-free (at the MRCI-F12+Q level), and with spin-orbit coupling at the CASSCF level (CAS-SO, see the theoretical methods section for full details). CAS-SO calculations at the equilibrium geometry provided a qualitatively similar picture to the MRCI-SO calculations, predicting that three A″ states were primarily responsible for the absorption, albeit with different transition dipole moments. The spin-free MRCI-F12+Q potential energy curves are shown in Figure 8(a), with symmetry labels assigned based on the energy ordering of the electronically excited states at the C_s equilibrium geometry. The lower energy states that correlate with CHICl + I products have A″ symmetry exclusively and are repulsive, although for the 2³A″ state this results from a conical intersection with the 1³A′ state at slightly extended C–I bond lengths. The higher energy states are bound along the C–I coordinate and correlate with electronically excited CHICl radicals.

19

The CAS-SO potential energy curves are shown in Figure 8(b). For clarity, the higher energy states that do not influence the photochemistry in the range of experimental excitation energies are grayed out. The three CAS-SO states equivalent to those carrying the greatest oscillator strengths in the MRCI-SO calculations are emboldened. The 2A″ and 3A″ states are repulsive and correlate with CHICl + I and CHICl + I*, respectively, while the 4A″ state is bound and correlates with electronically excited radicals. The 2A″ state has predominantly singlet character and is equivalent to the 1^1A″ state in the spin-free calculations. The higher energy 3A″ and 4A″ states, however, contain significant triplet character, as indicated in Table 3.

Bimodal and unimodal E_T distributions for I and I* atoms, respectively have also been observed in the near-UV photochemistry of CH_2I_2.[18,24] One possible explanation for this bimodality is the splitting of spin-orbit excited CHICl*, although no theoretical evidence was seen to confirm formation of CHIClI*. Toulson et al. did not observe spin-orbit splitting for the CH_2I radical after photodissociation of CH_2I_2. They suggested that either the spin-orbit coupling is much smaller than predicted or no spin-orbit excited CH_2I was produced.[18] Spin-orbit coupling constants (A_{SO}) in the CH_2I and CH_2Cl radicals have previously been derived from spectroscopic data and found to be 1392 cm^{-1} (0.17 eV)[80] and 116 cm^{-1} (0.014 eV),[81] respectively. The coupling constant in CH_2Cl is 12 times smaller than for CH_2I, suggesting that the addition of a chlorine atom would have a minor effect on the spin-orbit coupling in CHCII. It is unlikely that spin-orbit splitting of the radical accounts for the bimodal distributions. Xu et al. suggested that the slower components of the E_T distributions obtained probing I atoms arose from direct excitation to a repulsive surface while the faster component resulted from a curve crossing mechanism following initial excitation to a state that correlated with I* prodcuts.[24] This interpretation was based on the faster I atoms and the I* atoms having the same $\langle \beta \rangle$, while the slower I atoms had a smaller $\langle \beta \rangle$. The E_T-dependent anisotropy parameters obtained for CHI_2Cl photolysis show a similar trend, although the distinction between the faster and slower components for I atoms is less clear. In the context of the CAS-SO curves for CHI_2Cl, the equivalent mechanism

would involve I* atoms being formed after direct excitation to the 3A″ surface, with a subset undergoing a surface hop to a lower lying surface correlating to ground state I atoms. The slower component in the I atom E_T distribution would then result from direct excitation to and dissociation on the 2A″ surface. We note that the faster component of the I atom E_T distributions and the I* E_T distributions also result in the same fraction of E_{AVL} being partitioned into translation, $f_T \approx 0.29$. The absence of any measurable I* signal, yet still a bimodal E_T distribution for I atoms at longer photolysis wavelengths, would suggest that the probability of surface hopping from the 3A″ state is near unity at lower excitation energies and decreases as the excitation energy is increased. The slight increase in the fractional contribution of the faster component at shorter photolysis wavelengths, could be explained by preferential excitation to the 3A″ state over the 2A″ state, even as the hopping probability decreases.

In opposition to this mechanism, we note that the CAS-SO potential energy curves do not show any obvious crossings between the 3A″ surface and lower energy states correlating with CHICl + I products. Furthermore, as noted by Merrill *et al.* discussing CHBrCl$_2$ photochemistry,[82] the curve crossing mechanism might be expected to enhance vibrational excitation of the radical leading to slower fragments, while the angular anisotropies for CHI$_2$Cl imply that the faster I fragments results from trajectories that began on the 3A″ surface. However, the CAS-SO curves are one-dimensional cuts through the multidimensional potential energy surface, which dictates the energy disposal while the lack of symmetry resulting from any deviation from the equilibrium geometry will allow nonadiabatic interactions between the electronically excited states. Multidimensional curves would be needed to further understand the origin of this crossing and ultimately the energy disposal.

3. ClCHOO absorption spectrum

Single pass transient absorption spectroscopy was used to measure the absorption spectrum of ClCHOO in the 345–440 nm wavelength range using the same approach as our previous work on

CH$_2$OO.[44] Photolysis of CHI$_2$Cl at 355 nm and 266 nm was used to generate CHICl radicals in a 50 cm flow cell. Photolysis at 266 nm required different beam steering dichroic mirrors and allowed measurements to be extended slightly further to the blue, although the measurements are limited by the availability of sufficiently bright LEDs in the UV. Strong time-dependent absorbance of the LED probe light was observed only with the photolysis laser on and with O$_2$ present in flow cell. Significant absorbance due to IO was observed at longer (~100 µs) photolysis–probe delays while the non-IO absorbance reached a maximum after around 30 µs. The relative appearance times are similar to those in the CH$_2$I + O$_2$ reaction, where maximum concentrations of IO and CH$_2$OO were reached after approximately 100 µs and 10 µs, respectively. IO is known to be a minor product of the CH$_2$I + O$_2$ reaction at low pressure, and is formed both directly and as a result of the secondary reaction between CH$_2$OO and I atoms.[40,83] For the CHICl + O$_2$ reaction, formation of the Criegee intermediate appears to be somewhat slower and the appearance of IO at longer times is consistent with it being formed primarily by secondary reactions (e.g. ClCHOO + I → ClCHO + IO). Figure 9 shows the resulting absorption spectrum, attributed to ClCHOO, alongside that of CH$_2$OO after subtraction of the IO contribution.

Conversion of the measured absorbance to an absolute absorption cross section for ClCHOO as shown in Figure 9 requires an estimate of the number density present in the flow cell. The same approach used previously to determine the wavelength-dependent absorption cross section for CH$_2$OO,[44] which gave results in excellent agreement with independently calibrated measurements.[43] First, the initial CHICl number density is determined from that of the precursor CHI$_2$Cl, measured directly by single-pass absorption, and the photolysis laser fluence, assuming a unit quantum yield. Two estimates are required to obtain the concentration of ClCHOO: the yield for this product from the CHICl + O$_2$ reaction and a correction factor to account for the time dependence. We determine the latter empirically from transient absorption measurements, and assume the former is the same as that determined previously for the pressure-dependent CH$_2$OO yield of the CH$_2$I + O$_2$ reaction. The

estimated ClCHOO yield is the most important approximation and could lead to a (readily corrected) systematic error in the reported absorption cross section. With this caveat, it appears that the magnitude of the ClCHOO absorption cross section is comparable to that of CH_2OO in the wavelength region studied. It is clear from Figure 9, however, that the band maximum lies to wavelengths shorter than 345 nm.

The absorption spectrum of CH_2OO shows distinctive vibrational structure, with a clear progression of diffuse bands separated by 610 ± 40 cm^{-1}. The first band at $\sim$432 nm was tentatively assigned as the origin.[44] Recently, Ting and Lin have reported the absorption spectrum of the deuterated Criegee intermediate, CD_2OO, finding significant isotope shifts.[84] Calculations suggest that CH_2OO maintains its planar structure following excitation to the $\tilde{B}^1A'$ state, with the major geometric changes being contraction of the CO bond, extension of the OO bond and a decrease in the COO bond angle.[85,86] However, projections of the ground state vibrational wavefunctions, calculated at the MR-PT2 level, onto the $\tilde{B}$ state surface, suggested that three modes comprising the out-of-plane CH_2 wag, CH_2 scissors + CO stretch, and OO stretch are Franck-Condon active and are largely responsible for the structure in the absorption spectrum, in agreement with experiment.[86] In contrast, the absorption spectrum of ClCHOO shows far weaker structure. Following Ting and Lin, the absorption spectra are heavily smoothed and subtracted from the higher resolution data; the residuals are shown in Figure 9. The CH_2OO residual shows highly oscillatory structure resulting from the vibrational progression. Weaker oscillations are observed in the ClCHOO residual. The first band appears at $\sim$398 nm and the average peak-to-peak separation is 640 ± 60 cm^{-1}. The absorption spectra of the methyl-substituted Criegee intermediates CH_3CHOO and $(CH_3)_2COO$ are also largely featureless.[87,88]

ClCHOO can exist as two conformers, which can be labelled *syn* and *anti*, following the notation established for CH_3CHOO according to the OOCCl torsion angle. Single point EOM-CCSD/aug-cc-pVTZ calculations have been performed at the ground state geometry to explore the effect of the Cl atom

on the low-lying electronically excited states of both conformers relative to those of CH_2OO. Table 4 summarizes the results. The presence of the Cl atom has a marked effect on the vertical excitation energy, increasing that of the *syn*-ClCHOO conformer by 0.21 eV and decreasing that of *anti*-ClCHOO by 0.25 eV, with respect to CH_2OO. The oscillator strengths are the same for all three. The absorption maximum for the $\tilde{B}$–$\tilde{X}$ transition of CH_2OO is ~343 nm, and via the reflection principle can be considered to approximate the vertical excitation energy (3.61 eV). The EOM-CCSD calculations predict a vertical excitation energy that is around a third of an eV too high for CH_2OO. Assuming the same offset for ClCHOO, we predict respective absorption maxima of 324 nm and 368 nm for the *syn*-ClCHOO and *anti*-ClCHOO conformers. While the band maximum is not directly observed in our measurements, it clearly must lie at $\lambda < 345$ nm, implying that the spectrum is predominantly that of the *syn*-ClCHOO conformer. The wavelength for the band maximum predicted for *anti*-ClCHOO lies within the spectral range examined, but the band appears not to extend far enough to the red. *syn*-ClCHOO is predicted to be lower in energy by 0.07 eV at the CCSD/aug-cc-pVTZ level (including zero-point corrections), consistent with the value obtained by Cabezas *et al.* at the CCSD(T)-F12/aug-cc-PVTZ level.[49] It is not clear why such a small energy difference would lead to formation of the *syn* conformer being favored in a room temperature sample.

4. Atmospheric implications

The CHI_2Cl absorption spectrum overlaps significantly with the solar spectrum. The photolysis rate has been calculated using the equation:

$$J = \int F(\lambda)\sigma(\lambda)\phi(\lambda)d\lambda$$

where $F(\lambda)$ is the actinic flux at sea-level, $\sigma(\lambda)$ is the absorption cross section of CHI_2Cl. The photolysis quantum yield $\phi(\lambda)$ is assumed to be unity at all wavelengths. The actinic flux at a solar zenith angle of 0° is shown alongside the CHI_2Cl spectrum in Figure 1. The photolysis rate has been

24

calculated at the seawater surface for solar zenith angles between 0° and 60°, assuming an 80% albedo.[89] The values range from $(1.6–0.8)\times10^{-2}$ s^{-1} yielding lifetimes of 1–2 minutes. These values are around half of that calculated for CH_2I_2,[16] and are primarily due to the absorption spectrum extending to longer wavelengths and overlapping better with the solar spectrum, which compensates for the apparent decrease in the maximum absorption cross section of the A and B bands. Reactive sinks in the marine boundary layer are likely to be Cl and OH radicals. The lifetime of CH_2I_2 due to reaction with either Cl and OH radicals is estimated to be 46 and 62 hours, respectively.[90,91] If the reactivity for CHI_2Cl is similar to that of CH_2I_2, photolysis is likely to be the major gas-phase sink for CHI_2Cl produced in surface seawater.

Photolysis of CHI_2Cl leads to the formation of internally excited CHICl radicals and I/I* atom products. The role of I atom chemistry in the troposphere has been investigated extensively.[2,3] Haloalkyl fragments also play a role in atmospheric chemistry as they are generally thought to form peroxy radicals after reacting with O_2.[37] As with the CH_2I radical, reaction of the CHICl radical with O_2 appears to forms a carbonyl oxide or Criegee intermediate in comparably high yield. Pressure-dependent measurements of the $CH_2I + O_2$ reaction indicate a CH_2OO yield of 77% at 15 Torr (the pressure used in the measurement of the ClCHOO absorption cross section), decreasing to around 30% at atmospheric pressure.[40] It is difficult to estimate how much CHI_2Cl is present in the MBL due to its incredibly short lifetime and lack of field measurements. Carpenter *et al.* found that of the haloalkanes released by brown algae from Mace Head, Ireland, a maximum of 14% was CHI_2Cl compared to 35% CH_2I_2 and 51% CH_3I.[4] Additional measurements based on flux rates from the reactions between iodide, dissolved organic matter, and ozone, show that CHI_2Cl reaches a maximum of 6% of total haloalkane, when the production of CH_2I_2 and CH_3I are minimal.[6] Although only a small amount of CHI_2Cl is likely to be present in the MBL, the most probable removal mechanism is photolysis.

25

Conclusions

CHI$_2$Cl has been synthesized and the UV absorption spectrum measured. The spectrum is qualitatively like that of CH$_2$I$_2$, but is shifted to longer wavelengths and it is likely that photolysis will be the dominant removal mechanism during daylight hours in the MBL. The photodissociation dynamics of CHI$_2$Cl has been investigated in detail at several wavelengths spanning the first three absorption bands using DC slice velocity-map imaging. Images of I and I* atoms, detected using single-photon VUV ionization and 2+1 REMPI, show that the available energy is mainly partitioned into internal excitation of the CHICl radical co-fragment. Analysis of the wavelength dependence of the total translational energy release results in a bond dissociation energy of 1.73 eV, which is weaker than typical C–I bond strengths. Anisotropy parameters extracted from the angular distributions approach the limiting value of +2 for a parallel transition, indicating prompt dissociation via excited states of A″ symmetry. High-level *ab initio* calculations support the assertion that transitions to states of A″ symmetry are primarily responsible for the features seen in the absorption spectrum. Reaction between CHICl and O$_2$ leads to the formation of a species that absorbs in the 345–440 nm wavelength range, that is assigned to the ClCHOO Criegee intermediate. Compared to CH$_2$OO, the presence of a chlorine atom shifts the peak of the absorption spectrum from ∼343 nm to a predicted peak absorption of 324 nm for the *syn*-ClCHOO conformer.

Acknowledgements

References

(1)   O'Dowd, C. D.; Jimenez, J. L.; Bahreini, R.; Flagan, R. C.; Seinfeld, J. H.; Hämeri, K.; Pirjola, L.; Kulmala, M.; Jennings, S. G.; Hoffmann, T. Marine Aerosol Formation from Biogenic Iodine Emissions. *Nature* **2002**, *417* (6889), 632–636.

(2)   Saiz-Lopez, A.; Plane, J. M. C.; Baker, A. R.; Carpenter, L. J.; von Glasow, R.; Gómez Martín, J. C.; McFiggans, G.; Saunders, R. W. Atmospheric Chemistry of Iodine. *Chem. Rev.* **2012**, *112* (3), 1773–1804.

(3)   Carpenter, L. J. Iodine in the Marine Boundary Layer. *Chem. Rev.* **2003**, *103* (12), 4953–4962.

(4)   Carpenter, L. J.; Malin, G.; Liss, P. S.; Küpper, F. C. Novel Biogenic Iodine-Containing Trihalomethanes and Other Short-Lived Halocarbons in the Coastal East Atlantic. *Global Biogeochem. Cy.* **2000**, *14* (4), 1191–1204.

(5)   Baker, A. R.; Tunnicliffe, C.; Jickells, T. D. Iodine Speciation and Deposition Fluxes from the Marine Atmosphere. *J. Geophys. Res. Atmos.* **2001**, *106* (D22), 28743–28749.

(6)   Martino, M.; Mills, G. P.; Woeltjen, J.; Liss, P. S. A New Source of Volatile Organoiodine Compounds in Surface Seawater. *Geophys. Res. Lett.* **2009**, *36* (1).

(7)   Gardiner, S. H.; Lipciuc, M. L.; Karsili, T. N. V.; Ashfold, M. N. R.; Vallance, C. Dynamics of the A-Band Ultraviolet Photodissociation of Methyl Iodide and Ethyl Iodide via Velocity-Map Imaging with "universal" Detection. *Phys. Chem. Chem. Phys.* **2015**, *17* (6), 4096–4106.

(8)   Kawasaki, M.; Lee, S. J.; Bersohn, R. Photodissociation of Molecular Beams of Methylene Iodide and Iodoform. *J. Chem. Phys.* **1975**, *63* (2), 809–814.

(9)   Schmitt, G.; Comes, F. J. Photolysis of CH_2I_2 and $1,1$-$C_2H_4I_2$ at 300 nm. *J. Photochem.* **1980**, *14* (2), 107–123.

(10)   Senapati, D.; Kavita, K.; Das, P. K. Photodissociation Dynamics of CH_2ICl at 222, 236, 266, 280, and ~304 nm. *J. Phys. Chem. A* **2002**, *106* (36), 8479–8482.

(11)   Senapati, D.; Das, P. K. $Cl^*(^2P_{1/2})$ Production Dynamics from Chloroiodomethane (CH_2ICl) in the Ultraviolet. *Chem. Phys. Lett.* **2004**, *393* (4–6), 535–538.

(12)   Zhang, C.-H.; Zhang, Y.; Zhang, S.; Zhang, B. Photodissociation Dynamics of Chloroiodomethane in the A-Band. *Acta Physico-Chimica Sinica* **2009**, *25* (8), 1708–1712.

(13)   Cheng, M.; Lin, D.; Hu, L.; Du, Y.; Zhu, Q. Photodissociation Dynamics of $ICH_2Cl \rightarrow CH_2Cl + I^*/I$: Photofragment Translational Spectroscopy at 304 and 277 nm. *Phys. Chem. Chem. Phys.* **2016**, *18* (4), 3165–3172.

(14)   Lee, S. J.; Bersohn, R. Photodissociation of a Molecule with Two Chromophores. Bromoiodomethane. *J. Phys. Chem.* **1982**, *86* (5), 728–730.

(15)   Butler, L. J.; Hintsa, E. J.; Shane, S. F.; Lee, Y. T. The Electronic State-selective Photodissociation of CH_2BrI at 248, 210, and 193 nm. *J. Chem. Phys.* **1987**, *86* (4), 2051–2074.

(16)   Mössinger, J. C.; Shallcross, D. E.; Cox, R. A. UV-VIS Absorption Cross-Sections and Atmospheric Lifetimes of CH_2Br_2, CH_2I_2 and CH_2BrI. *J. Chem. Soc., Faraday Trans.* **1998**, *94* (10), 1391–1396.

(17)   Roehl, C. M.; Burkholder, J. B.; Moortgat, G. K.; Ravishankara, A. R.; Crutzen, P. J. Temperature Dependence of UV Absorption Cross Sections and Atmospheric Implications of Several Alkyl Iodides. *J. Geophys. Res.* **1997**, *102* (D11), 12819–12829.

(18)   Toulson, B. W.; Alaniz, J. P.; Hill, J. G.; Murray, C. Near-UV Photodissociation Dynamics of CH_2I_2. *Phys. Chem. Chem. Phys.* **2016**, *18* (16), 11091–11103.

(19)   Liu, Y.-J.; De Vico, L.; Lindh, R.; Fang, W.-H. Spin-Orbit Ab Initio Investigation of the Ultraviolet Photolysis of Diiodomethane. *ChemPhysChem* **2007**, *8* (6), 890–898.

(20)   Baughcum, S. L.; Leone, S. R. Photofragmentation Infrared Emission Studies of Vibrationally Excited Free Radicals CH_3 and CH_2I. *J. Chem. Phys.* **1980**, *72* (12), 6531–6545.

(21)   Koffend, J. B.; Leone, S. R. Tunable Laser Photodissociation: Quantum Yield of $I^*(^2P_{1/2})$ from CH_2I_2. *Chem. Phys. Lett.* **1981**, *81* (1), 136–141.

(22)   Hunter, T. F.; Kristjansson, K. S. Yield of $I(^2P_{1/2})$ in the Photodissociation of CH_2I_2. *Chem. Phys. Lett.* **1982**, *90* (1), 35–40.

(23)   Jung, K.-W.; Ahmadi, T. S.; El-Sayed, M. A. Photofragment Translational Spectroscopy of CH_2I_2 at 304 nm: Polarization Dependence and Energy Partitioning. *B. Korean Chem. Soc.* **1997**, *18* (12), 1274–1280.

(24)   Xu, H.; Guo, Y.; Liu, S.; Ma, X.; Dai, D.; Sha, G. Photodissociation Dynamics of CH_2I_2 Molecules in the Ultraviolet Range Studied by Ion Imaging. *J. Chem. Phys.* **2002**, *117* (12), 5722–5729.

(25)   Lehman, J. H.; Li, H.; Lester, M. I. Ion Imaging Studies of the Photodissociation Dynamics of CH_2I_2 at 248 nm. *Chem. Phys. Lett.* **2013**, *590*, 16–21.

(26)   Tarnovsky, A. N.; Alvarez, J.-L.; Yartsev, A. P.; Sundström, V.; Åkesson, E. Photodissociation Dynamics of Diiodomethane in Solution. *Chem. Phys. Lett.* **1999**, *312* (2–4), 121–130.

(27)   Zheng, X.; Phillips, D. L. Photoisomerization Reaction of CH_2BrI Following *A*-Band and *B*-Band Photoexcitation in the Solution Phase: Transient Resonance Raman Observation of the Iso-CH_2I–Br Photoproduct. *J. Chem. Phys.* **2000**, *113* (8), 3194–3203.

(28)   Kwok, W. M.; Ma, C.; Parker, A. W.; Phillips, D.; Towrie, M.; Matousek, P.; Zheng, X.; Phillips, D. L. Picosecond Time-Resolved Resonance Raman Observation of the Iso-CH_2Cl–I and Iso-CH_2I–Cl Photoproducts from The "photoisomerization" reactions of CH_2ICl in the Solution Phase. *J. Chem. Phys.* **2001**, *114* (17), 7536–7543.

(29)   Tarnovsky, A. N.; Sundström, V.; Åkesson, E.; Pascher, T. Photochemistry of Diiodomethane in Solution Studied by Femtosecond and Nanosecond Laser Photolysis. Formation and Dark Reactions of the CH_2I–I Isomer Photoproduct and Its Role in Cyclopropanation of Olefins. *J. Phys. Chem. A* **2004**, *108* (2), 237–249.

(30)   Saitow, K.; Naitoh, Y.; Tominaga, K.; Yoshihara, K. Photodissociation of CH_2I_2 and Subsequent Electron Transfer in Solution. *Chem. Asian J.* **2008**, *3* (4), 696–709.

(31)   Criegee, R. Mechanism of Ozonolysis. *Angew. Chem. Int. Ed.* **1975**, *14* (11), 745–752.

(32)   Hatakeyama, S.; Akimoto, H. Reactions of Criegee Intermediates in the Gas Phase. *Res. Chem. Intermediat.* **1994**, *20* (3–5), 503–524.

(33)   Johnson, D.; Marston, G. The Gas-Phase Ozonolysis of Unsaturated Volatile Organic Compounds in the Troposphere. *Chem. Soc. Rev.* **2008**, *37* (4), 699–716.

(34)   Taatjes, C. A.; Shallcross, D. E.; Percival, C. J. Research Frontiers in the Chemistry of Criegee Intermediates and Tropospheric Ozonolysis. *Phys. Chem. Chem. Phys.* **2014**, *16* (5), 1704–1718.

(35)   Osborn, D. L.; Taatjes, C. A. The Physical Chemistry of Criegee Intermediates in the Gas Phase. *Int. Rev. Phys. Chem.* **2015**, *34* (3), 309–360.

(36)   Welz, O.; Savee, J. D.; Osborn, D. L.; Vasu, S. S.; Percival, C. J.; Shallcross, D. E.; Taatjes, C. A. Direct Kinetic Measurements of Criegee Intermediate (CH_2OO) Formed by Reaction of CH_2I with O_2. *Science* **2012**, *335* (6065), 204–207.

(37)   Eskola, A. J.; Wojcik-Pastuszka, D.; Ratajczak, E.; Timonen, R. S. Kinetics of the Reactions of CH_2Br and CH_2I Radicals with Molecular Oxygen at Atmospheric Temperatures. *Phys. Chem. Chem. Phys.* **2006**, *8* (12), 1416–1424.

(38)   Huang, H.; Eskola, A. J.; Taatjes, C. A. Pressure-Dependent I-Atom Yield in the Reaction of CH_2I with O_2 Shows a Remarkable Apparent Third-Body Efficiency for O_2. *J. Phys. Chem. Lett.* **2012**, *3* (22), 3399–3403.

(39)   Stone, D.; Blitz, M.; Daubney, L.; Ingham, T.; Seakins, P. CH_2OO Criegee Biradical Yields Following Photolysis of CH_2I_2 in O_2. *Phys. Chem. Chem. Phys.* **2013**, *15* (44), 19119.

(40)   Ting, W.-L.; Chang, C.-H.; Lee, Y.-F.; Matsui, H.; Lee, Y.-P.; Lin, J. J.-M. Detailed Mechanism of the CH_2I + O_2 Reaction: Yield and Self-Reaction of the Simplest Criegee Intermediate CH_2OO. *J. Chem. Phys.* **2014**, *141* (10), 104308.

(41)   Beames, J. M.; Liu, F.; Lu, L.; Lester, M. I. Ultraviolet Spectrum and Photochemistry of the Simplest Criegee Intermediate CH_2OO. *J. Am. Chem. Soc.* **2012**, *134* (49), 20045–20048.

(42)   Sheps, L. Absolute Ultraviolet Absorption Spectrum of a Criegee Intermediate CH_2OO. *J. Phys. Chem. Lett.* **2013**, *4* (24), 4201–4205.

(43)   Ting, W.-L.; Chen, Y.-H.; Chao, W.; Smith, M. C.; Lin, J. J.-M. The UV Absorption Spectrum of the Simplest Criegee Intermediate CH_2OO. *Phys. Chem. Chem. Phys.* **2014**, *16* (22), 10438–10443.

28

(44) Foreman, E. S.; Kapnas, K. M.; Jou, Y.; Kalinowski, J.; Feng, D.; Gerber, R. B.; Murray, C. High Resolution Absolute Absorption Cross Sections of the $\tilde{B}^1A'–\tilde{X}^1A'$ Transition of the CH_2OO Biradical. *Phys. Chem. Chem. Phys.* **2015**, *17* (48), 32539–32546.

(45) Beames, J. M.; Liu, F.; Lu, L.; Lester, M. I. UV Spectroscopic Characterization of an Alkyl Substituted Criegee Intermediate CH_3CHOO. *J. Chem. Phys.* **2013**, *138* (24), 244307-244307–244309.

(46) Liu, F.; Beames, J. M.; Green, A. M.; Lester, M. I. UV Spectroscopic Characterization of Dimethyl- and Ethyl-Substituted Carbonyl Oxides. *J. Phys. Chem. A* **2014**, *118* (12), 2298–2306.

(47) Niki, H.; Maker, P. D.; Savage, C. M.; Breitenbach, L. P. Atmospheric Ozone-Olefin Reactions. *Environ. Sci. Technol.* **1983**, *17* (7), 312A–322A.

(48) Burkholder, J. B.; Cox, R. A.; Ravishankara, A. R. Atmospheric Degradation of Ozone Depleting Substances, Their Substitutes, and Related Species. *Chem. Rev.* **2015**, *115* (10), 3704–3759.

(49) Cabezas, C.; Guillemin, J.-C.; Endo, Y. Fourier-Transform Microwave Spectroscopy of a Halogen Substituted Criegee Intermediate ClCHOO. *J. Chem. Phys.* **2016**, *145* (18), 184304.

(50) Kawabata, N.; Tanimoto, M.; Fujiwara, S. Synthesis of Monohalocyclopropane Derivatives from Olefins by the Reaction with Trihalomethanes and Copper. *Tetrahedron* **1979**, *35* (16), 1919–1923.

(51) Jones, G. B.; Chapman, B. J. Chlorodiiodomethane. In *Encyclopedia of Reagents for Organic Synthesis*; John Wiley & Sons, Ltd, 2001.

(52) Li, D. B.; Ng, S.-C.; Novak, I. Novel Synthetic Approaches to CHBrFI, CHClFI and CHBrClI. *Tetrahedron* **2002**, *58* (29), 5923–5926.

(53) Foreman, E. S.; Kapnas, K. M.; Murray, C. Reactions between Criegee Intermediates and the Inorganic Acids HCl and HNO_3 : Kinetics and Atmospheric Implications. *Angew. Chem. Int. Ed.* **2016**, *55* (35), 10419–10422.

(54) Adler, T. B.; Knizia, G.; Werner, H.-J. A Simple and Efficient CCSD(T)-F12 Approximation. *J. Chem. Phys.* **2007**, *127* (22), 221106.

(55) Knizia, G.; Adler, T. B.; Werner, H.-J. Simplified CCSD(T)-F12 Methods: Theory and Benchmarks. *J. Chem. Phys.* **2009**, *130* (5), 054104.

(56) Peterson, K. A.; Adler, T. B.; Werner, H.-J. Systematically Convergent Basis Sets for Explicitly Correlated Wavefunctions: The Atoms H, He, B–Ne, and Al–Ar. *J. Chem. Phys.* **2008**, *128* (8), 084102.

(57) Hill, J. G.; Peterson, K. A. Correlation Consistent Basis Sets for Explicitly Correlated Wavefunctions: Pseudopotential-Based Basis Sets for the Post-D Main Group Elements Ga–Rn. *J. Chem. Phys.* **2014**, *141* (9), 094106.

(58) Peterson, K. A.; Shepler, B. C.; Figgen, D.; Stoll, H. On the Spectroscopic and Thermochemical Properties of ClO, BrO, IO, and Their Anions. *J. Phys. Chem. A* **2006**, *110* (51), 13877–13883.

(59) Kritikou, S.; Hill, J. G. Auxiliary Basis Sets for Density Fitting in Explicitly Correlated Calculations: The Atoms H–Ar. *J. Chem. Theory Comput.* **2015**, *11* (11), 5269–5276.

(60) Yousaf, K. E.; Peterson, K. A. Optimized Auxiliary Basis Sets for Explicitly Correlated Methods. *J. Chem. Phys.* **2008**, *129* (18), 184108.

(61) Valeev, E. F. Improving on the Resolution of the Identity in Linear R12 Ab Initio Theories. *Chem. Phys. Lett.* **2004**, *395* (4–6), 190–195.

(62) Shiozaki, T.; Werner, H.-J. Communication: Second-Order Multireference Perturbation Theory with Explicit Correlation: CASPT2-F12. *J. Chem. Phys.* **2010**, *133* (14), 141103.

(63) Shiozaki, T.; Knizia, G.; Werner, H.-J. Explicitly Correlated Multireference Configuration Interaction: MRCI-F12. *J. Chem. Phys.* **2011**, *134* (3), 034113.

(64) Shiozaki, T.; Werner, H.-J. Explicitly Correlated Multireference Configuration Interaction with Multiple Reference Functions: Avoided Crossings and Conical Intersections. *J. Chem. Phys.* **2011**, *134* (18), 184104.

(65) Davidson, E. R.; Silver, D. W. Size Consistency in the Dilute Helium Gas Electronic Structure. *Chem. Phys. Lett.* **1977**, *52* (3), 403–406.

(66) Dunning Jr., T. H. Gaussian Basis Sets for Use in Correlated Molecular Calculations. I. The Atoms Boron through Neon and Hydrogen. *J. Chem. Phys.* **1989**, *90* (2), 1007–1023.

(67) Dunning, T. H.; Peterson, K. A.; Wilson, A. K. Gaussian Basis Sets for Use in Correlated Molecular Calculations. X. The Atoms Aluminum through Argon Revisited. *J. Chem. Phys.* **2001**, *114* (21), 9244–9253.

(68) Werner, H.-J.; Knowles, P. J.; Knizia, G.; Manby, F. R.; Schütz, M. Molpro: A General-Purpose Quantum Chemistry Program Package. *Comput. Mol. Sci.* **2012**, *2* (2), 242–253.

(69) MOLPRO, Version 2015.1, a Package of Ab Initio Programs, H.-J. Werner, P. J. Knowles, G. Knizia, F. R. Manby, M. Schütz, P. Celani, W. Györffy, D. Kats, T. Korona, R. Lindh, A. Mitrushenkov, G. Rauhut, K. R. Shamasundar, T. B. Adler, R. D. Amos, A. Bernhardsson, A. Berning, D. L. Cooper, M. J. O. Deegan, A. J. Dobbyn, F. Eckert, E. Goll, C. Hampel, A. Hesselmann, G. Hetzer, T. Hrenar, G. Jansen, C. Köppl, Y. Liu, A. W. Lloyd, R. A. Mata, A. J. May, S. J. McNicholas, W. Meyer, M. E. Mura, A. Nicklass, D. P. O'Neill, P. Palmieri, D. Peng, K. Pflüger, R. Pitzer, M. Reiher, T. Shiozaki, H. Stoll, A. J. Stone, R. Tarroni, T. Thorsteinsson, and M. Wang, See http://www.molpro.net.

(70) Novak, I.; Li, D. B.; Potts, A. W.; Shareef, A.; Kovač, B. Halogen–Halogen Interactions in Halomethanes. *J. Org. Chem.* **2002**, *67* (10), 3510–3513.

(71) von Niessen, W.; Åsbrink, L.; Bieri, G. 30.4 nm He (II) Photoelectron Spectra of Organic Molecules Part VI. Halogeno-Compounds (C, H, X; X = Cl, Br, I). *J. Electron. Spectrosc.* **1982**, *26* (2), 173–201.

(72) Fan, H.; Pratt, S. T. Determination of Spin–Orbit Branching Fractions in the Photodissociation of Halogenated Hydrocarbons. *J. Phys. Chem. A* **2007**, *111* (19), 3901–3906.

(73) Gardiner, S. H.; Lipciuc, M. L.; Karsili, T. N. V.; Ashfold, M. N. R.; Vallance, C. Dynamics of the A-Band Ultraviolet Photodissociation of Methyl Iodide and Ethyl Iodide via Velocity-Map Imaging with "universal" Detection. *Phys. Chem. Chem. Phys.* **2015**, *17* (6), 4096–4106.

(74) Lago, A. F.; Kercher, J. P.; Bödi, A.; Sztáray, B.; Miller, B.; Wurzelmann, D.; Baer, T. Dissociative Photoionization and Thermochemistry of Dihalomethane Compounds Studied by Threshold Photoelectron Photoion Coincidence Spectroscopy. *J. Phys. Chem. A* **2005**, *109* (9), 1802–1809.

(75) Busch, G. E.; Wilson, K. R. Triatomic Photofragment Spectra. I. Energy Partitioning in NO_2 Photodissociation. *J. Chem. Phys.* **1972**, *56* (7), 3626–3638.

(76) Ratliff, B. J.; Womack, C. C.; Tang, X. N.; Landau, W. M.; Butler, L. J.; Szpunar, D. E. Modeling the Rovibrationally Excited C_2H_4OH Radicals from the Photodissociation of 2-Bromoethanol at 193 nm. *J. Phys. Chem. A* **2010**, *114* (14), 4934–4945.

(77) McKown, B. G.; Ceriotti, M.; Womack, C. C.; Kamarchik, E.; Butler, L. J.; Bowman, J. M. Effects of High Angular Momentum on the Unimolecular Dissociation of CD_2CD_2OH: Theory and Comparisons with Experiment. *J. Phys. Chem. A* **2013**, *117* (42), 10951–10963.

(78) Kisiel, Z. *Principal Moments of Inertia From STructure*.

(79) Demyanenko, A. V.; Dribinski, V.; Reisler, H.; Meyer, H.; Qian, C. X. W. Product Quantum-State-Dependent Anisotropies in Photoinitiated Unimolecular Decomposition. *J. Chem. Phys.* **1999**, *111* (16), 7383.

(80) Bailleux, S.; Kania, P.; Skřínský, J.; Okabayashi, T.; Tanimoto, M.; Matsumoto, S.; Ozeki, H. Hyperfine Resolved Fourier Transform Microwave and Millimeter-Wave Spectroscopy of the Iodomethyl Radical, CH_2I ($\tilde{X}^2B_1$). *J. Phys. Chem. A* **2010**, *114* (14), 4776–4784.

(81) Endo, Y.; Saito, S.; Hirota, E. The Microwave Spectrum of the Chloromethyl Radical, CH_2Cl. *Can. J. Phys.* **1984**, *62* (12), 1347–1360.

(82) Merrill, W. G.; Crim, F. F.; Case, A. S. Dynamics and Yields for $CHBrCl_2$ Photodissociation from 215–265 nm. *Phys. Chem. Chem. Phys.* **2016**, *18* (48), 32999–33008.

30

(83) Foreman, E. S.; Murray, C. Kinetics of IO Production in the $CH_2I + O_2$ Reaction Studied by Cavity Ring-Down Spectroscopy. *J. Phys. Chem. A* **2015**, *119* (34), 8981–8990.

(84) Ting, A. W.-L.; Lin, J. J.-M. UV Spectrum of the Simplest Deuterated Criegee Intermediate CD_2OO. *J. Chin. Chem. Soc.* **2017**, *64* (4), 360–368.

(85) Dawes, R.; Jiang, B.; Guo, H. UV Absorption Spectrum and Photodissociation Channels of the Simplest Criegee Intermediate (CH_2OO). *J. Am. Chem. Soc.* **2015**, *137* (1), 50–53.

(86) Kalinowski, J.; Foreman, E. S.; Kapnas, K. M.; Murray, C.; Räsänen, M.; Gerber, R. B. Dynamics and Spectroscopy of CH_2OO Excited Electronic States. *Phys. Chem. Chem. Phys.* **2016**, *18* (16), 10941–10946.

(87) Smith, M. C.; Ting, W.-L.; Chang, C.-H.; Takahashi, K.; Boering, K. A.; Lin, J. J.-M. UV Absorption Spectrum of the C2 Criegee Intermediate CH_3CHOO. *J. Chem. Phys.* **2014**, *141* (7), 074302.

(88) Chang, Y.-P.; Chang, C.-H.; Takahashi, K.; Lin, J. J.-M. Absolute UV Absorption Cross Sections of Dimethyl Substituted Criegee Intermediate $(CH_3)_2COO$. *Chem. Phys. Lett.* **2016**, *653*, 155–160.

(89) Finlayson-Pitts, B. J.; Pitts, J. N. *Chemistry of the Upper and Lower Atmosphere: Theory, Experiments, and Applications*; Academic Press: San Diego, 2000.

(90) Zhang, S.; Strekowski, R.; Bosland, L.; Monod, A.; Zetzsch, C. Kinetic Study of the Reaction of OH with CH_2I_2. *Phys. Chem. Chem. Phys.* **2011**, *13* (24), 11671.

(91) Enami, S.; Hashimoto, S.; Kawasaki, M.; Nakano, Y.; Ishiwata, T.; Tonokura, K.; Wallington, T. J. Observation of Adducts in the Reaction of Cl Atoms with XCH_2I (X = H, CH_3, Cl, Br, I) Using Cavity Ring-Down Spectroscopy. *J. Phys. Chem. A* **2005**, *109* (8), 1587–1593.

Tables

Table 1. Experimental energy partioning for I and I* channels of CHI_2Cl photodissociation. $\langle E_{INT} \rangle$ is partitioned into $\langle E_R \rangle$ and $\langle E_V \rangle$ using the Butler and co-workers impulsive model described in the text. Anisotropy parameters are averaged over the E_T distributions.

	λ / nm	E_{AVL} / eV	$\langle E_T \rangle$ / eV	$\langle E_R \rangle$ / eV	$\langle E_V \rangle$ / eV	$\langle \beta \rangle$
	355.0	1.76	0.41	0.56	0.80	+0.79
	344.5	1.87	0.44	0.59	0.84	+0.82
I	304.3	2.34	0.54	0.73	1.07	+1.32
	281.7	2.67	0.63	0.86	1.18	+1.47
	266.0	2.93	0.68	0.93	1.31	+1.32
	344.6	0.93	0.28	0.39	0.26	+1.56
I*	304.0	1.41	0.38	0.53	0.49	+1.27
	281.8	1.73	0.51	0.70	0.51	+1.49

Table 2. Fractional energy partitioning into translation, rotation and vibration for CHI$_2$Cl photodissociation as predicted by the soft impulsive model of Busch and Wilson, or the modified impulsive model of Butler and co-workers (in parentheses), as discussed in the text.

	$f_{T,exp}$	f_T	f_R	f_v	$\mu b^2/I$
CH$_2$ICl	0.44	0.36	0.56 (0.48)	0.09 (0.16)	1.36
CH$_2$IBr	0.31	0.23	0.66 (0.59)	0.11 (0.18)	2.51
CH$_2$I$_2$	0.21	0.19	0.68 (0.62)	0.13 (0.19)	3.28
CHI$_2$Cl	0.26	0.15	(0.06)	(0.79)	0.38

Table 3. Spin-orbit coupled MRCI-F12+Q electronically excited state energies, transtion dipole moments and percentage triplet character calcaulted at the CCSD(T)-F12 equilibrium geometry.

State	#	$E-E_1$ / eV	TDM / D	% triplet
1 A′	1	0.000		99%
1 A″	13	3.768	0.116	16%
2 A″	14	4.066	0.819	96%
3 A″	15	4.466	0.526	46%
4 A″	16	4.734	0.835	55%
6 A″	18	5.262	0.092	100%
6 A'	6	5.293	0.083	99%
7 A'	7	5.489	0.067	94%

Table 4. EOM-CCSD/aug-cc-pVTZ calculations characterizing the $\tilde{B}^1A'–\tilde{X}^1A'$ transitions of the Criegee intermediates CH_2OO and CHClOO. Calculated (observed) wavelengths of the origin, λ_{origin}, the band maximum, λ_{max}, based on vertical excitation energies, and the oscillator strengths, f, are shown.

	λ_{origin} / nm	λ_{max} / nm	f
CH_2OO	343 (431)	314 (~343)	0.153
syn-ClCHOO	324 (<420 nm)	298 (<345)	0.159
anti-ClCHOO	368	335	0.158

Figures
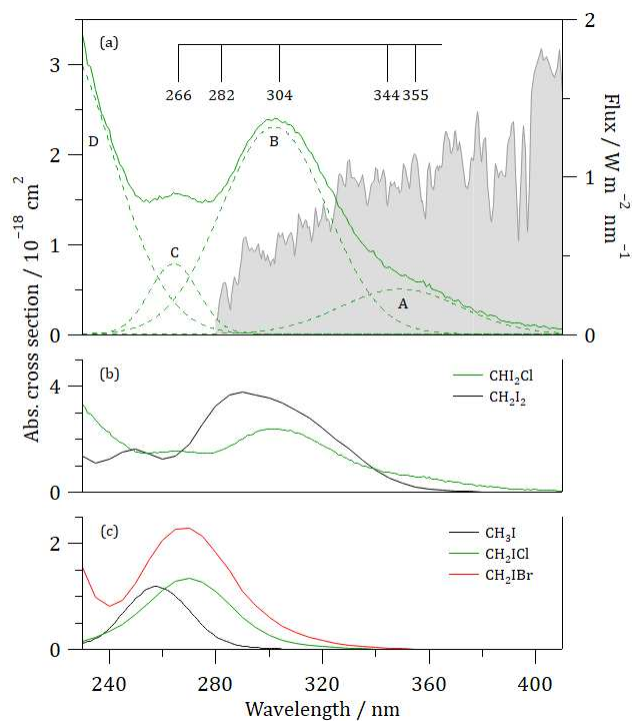
Figure 1. (a) Absorption spectrum for CHI$_2$Cl (green) at 295 K overlaid with individual Gaussian components (dashed) and AM1.5 solar irradiance spectrum (gray, shaded). The comb indicates the photolysis wavelengths used for ion imaging experiments. (b) Absorption spectra for CH$_2$I$_2$ (black, Mössinger *et al.*) and CHI$_2$Cl (this study). (c) Absorption spectra for CH$_3$I (black, Man *et al.*), CH$_2$ICl (green, Roehl *et al.*) and CH$_2$IBr (Mössinger *et al.*).
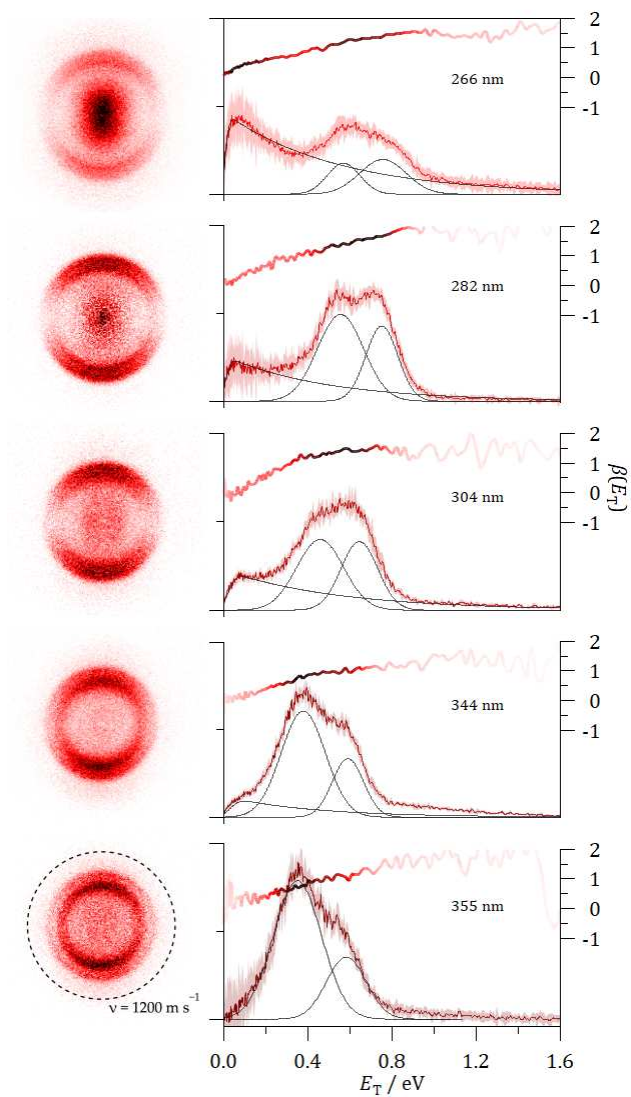
Figure 2. Ion images of I atom products following the photodissociation of CHI_2Cl at the indicated wavelengths and normalized translational energy distributions, $P(E_T)$. The individual components of the E_T distribution fits are shown as thin gray lines. E_T dependent anisotropy parameters, $\beta(E_T)$ are also shown, with the color scales weighted by the $P(E_T)$ distributions.
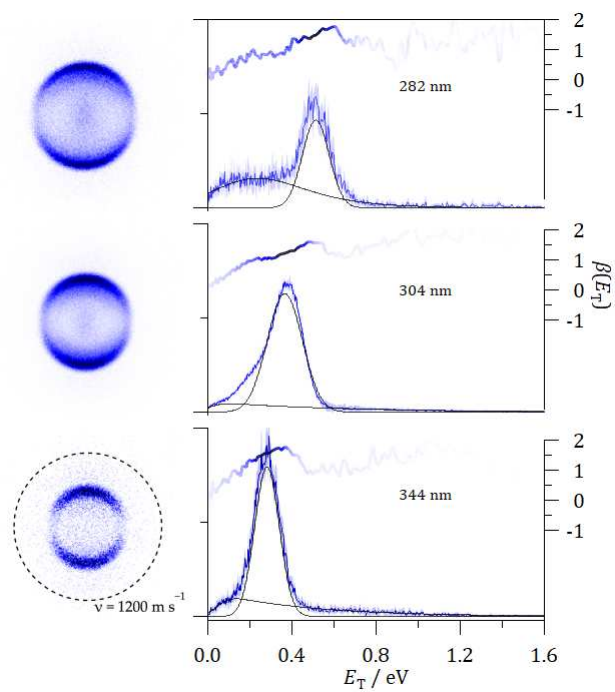
Figure 3. Ion images of I* atom products following the photodissociation of CHI$_2$Cl at the indicated wavelengths and normalized translational energy distributions, $P(E_T)$. The individual components of the E_T distribution fits are shown as thin gray lines. E_T dependent anisotropy parameters, $\beta(E_T)$ are also shown, with the color scales weighted by the $P(E_T)$ distributions.
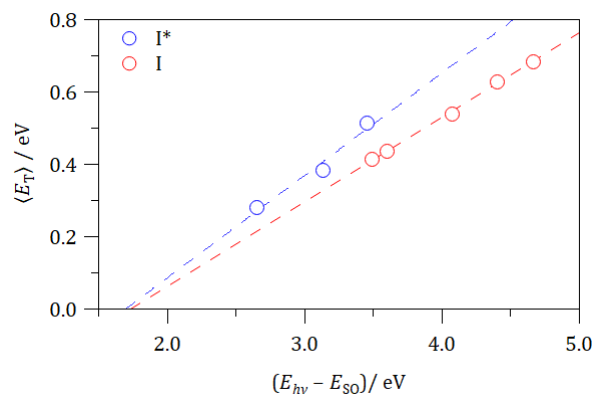
Figure 4. Average translational energies, $\langle E_T \rangle$, plotted as function of the difference between the photolysis photon energy, $E_{h\nu}$, and spin-orbit energy, E_{SO}, of the probed I/I* atoms. The *x*-intercept defines the bond dissociation energy.
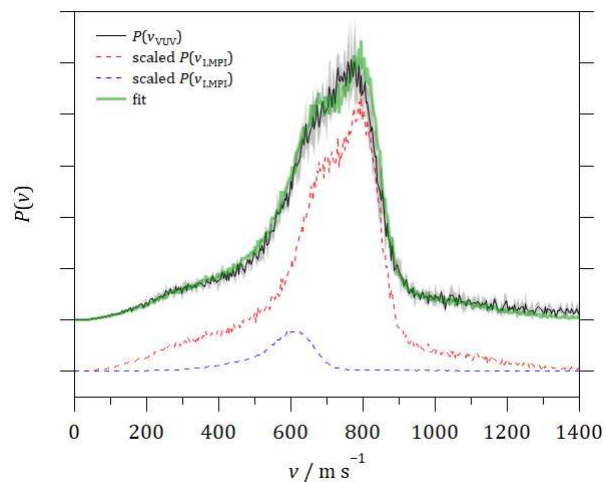
Figure 5. Decomposition of the iodine atom speed distribution obtained at a photolysis wavelength of 304 nm using VUV ionization (black). The best-fit fit linear combination of scaled state-selective I and I* speed distributions obtained using REMPI (dashed red and blue) is shown in green.
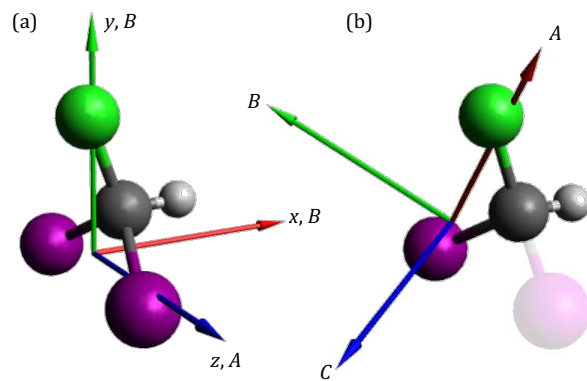
Figure 6. CHI$_2$Cl optimized geometry calculated at the CCSD(T)-F12b level. Principal inertial axes are indicated for the parent molecule and for the CHICl radical at the initial geometry, as used for the impulsive model calculations described in the text.
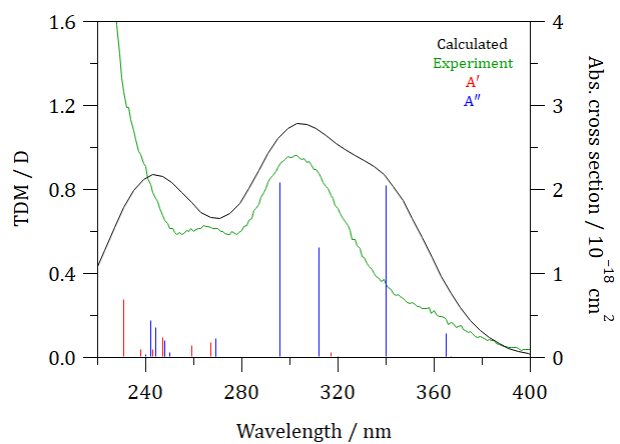
Figure 7. MRCI-F12+Q calculated (black) and experimental (green) absorption spectra for CHI$_2$Cl. The stick spectrum shows transition dipole moments plotted against vertical excitation energies for A$'$ (red) and A$''$ (blue) states. The vertical transitions have been broadened by a 20 nm FWHM Gaussian function and shifted 31 nm to longer wavelengths.
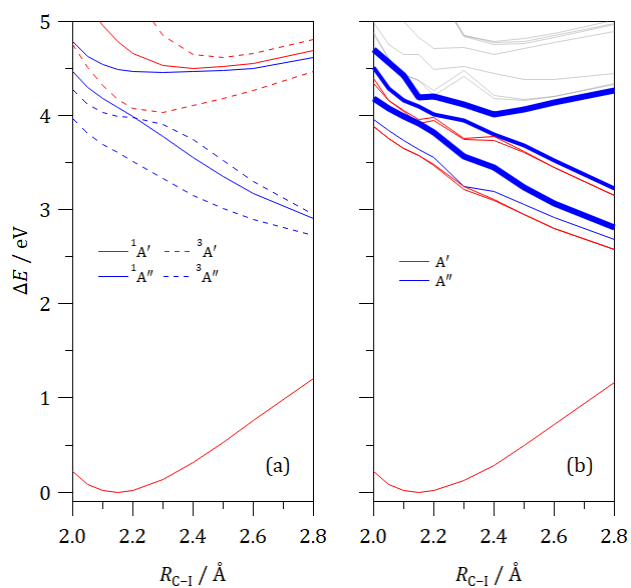
Figure 8. *Ab initio* potential energy curves (PECs) along the C–I bond coordinate for CHI$_2$Cl. (a) MRCI-F12+Q spin-free PECs, (b) CASSCF spin-orbit coupled PECs. Red curves are states with A$'$ symmetry at the C_s equilibrium geometry and blue curves are A$''$ symmetry. In panel (a) solid lines indicate singlet states, while dashed curves indicate triplet states. In panel (b), the states primarily responsible for the absorption spectrum are emboldened.
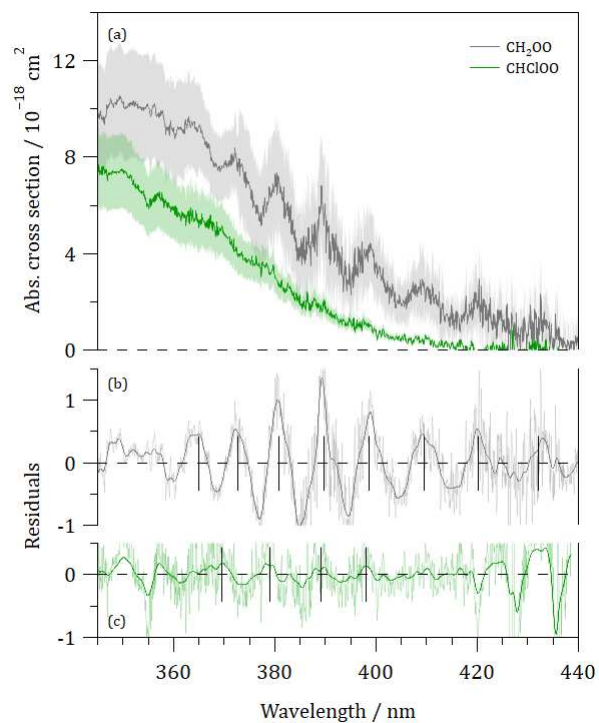
Figure 9. (a) UV absorption spectrum of ClCHOO (green) and CH₂OO (gray). (b) and (c) show the residuals after subtraction of a smoothed spectrum. The vertical lines indicate the positions of vibrational bands. The oscillations at $\lambda > 420$ nm in panel (c) arise from over-subtraction of the background IO absorbance.